ROYAL SOCIETY OF CHEMISTRY

PAPER

Check for updates

Capturing ammonium nitrate in a synthetic uranium oxide hydrate phase: revealing the role of ammonium ions and anion inclusions †

Yingjie Zhang, [ID] *[a] Timothy A. Ablott,[a] Maria K. Nicholas,[a] Inna Karatchevtseva[a] and Jakub Plášil [ID] [b]

Although uranium oxide hydrate (UOH) minerals and synthetic phases have been extensively studied, the role of ammonium ions in the formation of UOH materials is not well understood. In this work, the stabilization of a synthetic UOH phase with ammonium ions and the inclusion of ammonium nitrate were investigated using a range of structural and spectroscopic techniques. Compound $(NH_4)_2(NO_3)$ $[(UO_2)_3O_2(OH)_3]$ (**U-N1**) crystallises in the orthorhombic $Pmn2_1$ space group, having a layered structure with typical α-U_3O_8 type layers and interlayer $(NH_4)^+$ cations as well as $(NO_3)^-$ anions. The presence of uranyl, $(NH_4)^+$ cations and $(NO_3)^-$ anions were further confirmed with a combination of FTIR and Raman spectroscopies through characteristic vibrational modes. The roles of the $(NH_4)^+$ cations for charge compensation and facilitating the inclusion of $(NO_3)^-$ anions *via* hydrogen bonding were revealed and discussed. The findings have implications for uranium geochemistry, reprocessing of spent nuclear fuel and possible spent nuclear fuel alteration pathways under geological disposal.

1. Introduction

As the secondary uranium minerals formed in the early stage of uraninite (UO_{2+x}) weathering (oxidation and hydration), uranium oxide hydrate (UOH) minerals have attracted recent attention owing to them being direct natural analogues for the alterations of spent nuclear fuel (SNF) under geological disposal.[1–3] It is well understood that both uraninite, and therefore UO_2 (the key component of SNF), will gradually oxidise to U(VI) under oxidative conditions.[4–6] The uranyl $[(UO_2)^{2+}]$ cation, as a stable U(VI) form, can coordinate with O/OH ligands in the equatorial plane, forming tetragonal, pentagonal and hexagonal bipyramids as uranyl polyhedra that further connect to each other to form various uranyl oxyhydroxide layered structures with a variety of interlayer cations.[7–10] Apart from the two dozen known UOH minerals identified in various uranium deposits,[1,4] about the same but growing numbers of synthetic UOH compounds are being synthesised in the laboratory.[1–4] Most synthetic UOH materials have layered structures with uranium

oxide hydroxide layers and interlayer cations, differing mainly on O/OH ratio in the UOH layers and the interlayer cations. The UOH layer topologies have been widely reviewed.[11] In terms of secondary cations for the synthetic UOH materials, alkali and alkaline earth metal ions dominate.[12–18] However, UOHs with transition metals,[19–22] lead[23] and lanthanide ions[24–26] have also been studied and reported recently.

In addition to the dominant layered UOH structures, several other types of three-dimensional (3D) structures have also been revealed. Typical examples include complicated 3D architectures of UOH materials stabilized by Cs(I), Sr(II) and Ba(II) ions.[16,17,27] Furthermore, open framework structures known as uranium oxide hydrate frameworks (UOHFs) can be formed with uranyl pentagonal bipyramid dimers acting as bridging ligands linking the β-U_3O_8 type uranium oxide hydroxide layers.[28] These UOHFs have high structure flexibility and are capable of incorporating a range of additional cations from 1+ to 4+ valences including $(NH_4)^+$, Sr^{2+}, Y^{3+}, Er^{3+}, Sm^{3+}, Eu^{3+}, Gd^{3+} and U^{4+} in the framework channels,[29–32] highlighting the complex uranium hydrolysis chemistry in the presence of various secondary cations.

Ammonium nitrate (AN), $(NH_4)NO_3$, has been widely utilised in the nuclear industry.[33] Notably, production of UO_2 fuel for nuclear reactors requires the precipitation of ammonium di-uranate (ADU), which is facilitated by the addition of ammonia and AN, followed by calcination to UO_3 as the first uranium oxide. The quality and consistency of ADU precipitate

aAustralian Nuclear Science and Technology Organisation, Locked Bag 2001, Kirrawee DC, NSW 2232, Australia. E-mail: yzx@ansto.gov.au
bDepartment of Structure Analysis, Institute of Physics of the CAS, Na Slovance 2, Praha 8, 182 00, Czech Republic
†Electronic supplementary information (ESI) available: Supporting figures and tables. CCDC 2353965 (**U-N1**). For ESI and crystallographic data in CIF or other electronic format see DOI: https://doi.org/10.1039/d4dt01372g

are quite important in industrial operations.[34] The processing parameters such as solution pH, addition of ammonia and AN affect the particle size, crystal structure and characteristics of ADU,[35] and subsequently the properties of the UO_3.[36] As such, the effect of AN addition has been extensively investigated.[37] The wide applications of AN in the current uranium-based nuclear fuel cycle (NFC) leads to its presence in various steps of the NFC. Therefore, its further interactions with UO_3/UO_2 warrant additional research efforts.

In nature, high ammonium concentrations in mineralizing fluids are likely derived from the breakdown of organic matters in sediments within the hydrothermal system,[38] as well as from the bacterial activity (a process called DNRA – dissimilatory NO_3^- reduction to ammonium NH_{4+})[39] connected with the oxidative dissolution of primary sulfidic minerals. Consequently, it is often found in uranium-containing minerals such as uranyl sulphates and phosphates.[40] It is speculated that the key role of the ammonium ion would be the charge compensation, possibly replacing alkali ions. Even though the $(NH_4)^+$ ion has been found in nearly 15 uranyl minerals such as sulphates, phosphates etc.,[40] its exact role in the formation of UOH minerals and synthetic phases has not been understood. Only one synthetic UOH compound with ammonium ions was reported in the literature.[29] The compound (UOHF-NH_4), forming as needle-like crystals, was synthesized hydrothermally at 220 °C using uranyl oxyacetate and ammonium carbonate in water. The crystal structure contains β-U_3O_8-type sheets parallel to (001) cross-linked through U_2O_{12} pentagonal bipyramid dimers, resulting in an open framework structure composed only of uranium polyhedra. The $(NH_4)^+$ cations and H_2O molecules are located in the framework channels.[29] To our best knowledge, no layered structure of UOH minerals or synthetic phases with ammonium ions has been structurally documented.

What is also immediately apparent in reviewing the literature is that, despite the comprehensive studies on synthetic UOH materials with various cations across the periodic table, anion inclusions in synthetic UOH phases are much less studied.[41] In this work, we report the synthesis and characterisation of a new UOH compound containing $(NH_4)^+$ ions facilitating the inclusion of $(NO_3)^-$ anions. The layered structure with α-U_3O_8 type layers and interlayer $(NH_4)^+$ ions and $(NO_3)^-$ anions was revealed by synchrotron single crystal X-ray diffraction. Subsequently, the presence of uranyl species, $(NH_4)^+$ cations and $(NO_3)^-$ anions was further confirmed with a combination of FTIR and Raman spectroscopies. The roles of the $(NH_4)^+$ ions on the formation of layered UOH phases, e.g., charge compensation with interlayer hydrogen bonding and facilitating the inclusion of $(NO_3)^-$ anions, were explored and discussed. In addition, its electronic structure was also investigated and reported.

2. Experimental

2.1. Material synthesis

Uranyl nitrate hexahydrate with uranium in natural isotopic abundance was used. Materials containing uranium are radio-

active and should be handled with care in regulated facilities. Other chemicals in A.R. grade were purchased from Sigma-Aldrich (Merck).

$(NH_4)_2(NO_3)[(UO_2)_3O_2(OH)_3]$ **(U-N1).** Uranyl nitrate hexahydrate (0.083 g, 0.165 mmol) and ammonium nitrate (0.0264 g, 0.33 mmol) were dissolved in 5 mL deionised water (DIW), followed by adjusting the solution pH to 4.0 with a dilute NH_3 solution. The mixture was then transferred into a 30 mL Teflon vessel, sealed in a steel autoclave and heated in an oven at 180 °C for 72 h. Orange crystalline compound **U-N1** was obtained after cooling (5 °C h^{-1}) to ambient temperature with the final solution pH 2.84, washed with DIW and dried in air at ambient temperature, with 27 wt% yield (0.017 g). Further increasing solution pH leading to a final solution pH up to 4.0 can increase the yield, but also leads to the formation of an amorphous fine powder as a secondary phase.

2.2. Characterisation

Synchrotron single crystal X-ray diffraction. The single crystal data for compound **U-N1** (CCDC 2353965†) were collected at 100(2) K on the MX1 beamline[42] at the Australian Synchrotron employing silicon double crystal monochromated synchrotron radiation (λ = 0.71079 Å). Data integration and reduction were undertaken with XDS.[43] Absorption corrections were applied to the data using SADABS.[44] The structure was solved by SHELXT[45] and refined with SHELXL-2014[46] using the Olex^2 graphical user interface.[47] All but hydrogen atoms were located on the electron density map and refined anisotropically. Hydrogen atoms were added in the calculated positions for the ammonium ion and refined using a riding model. Potential hydrogen bonds and short molecular interactions were calculated with PLATON.[48]

Scanning electron microscopy (SEM). The crystal morphologies and elemental compositions were analysed using SEM coupled with energy dispersive spectrometry (EDS). Samples were carbon coated and examined in a Zeiss Ultra Plus SEM (Carl Zeiss NTS GmbH, Oberkochen, Germany) operating at 15 kV equipped with an Oxford Instruments X-Max 80 mm^2 SDD X-ray microanalysis system.

Powder X-ray diffraction (PXRD). PXRD patterns were collected on a Bruker D8 Focus diffractometer equipped with Cu-Kα (λ = 1.5418 Å) radiation in the angle range of 5–80° 2θ with a step size of 0.02° (2θ). The room temperature pattern was performed with a data collection time of 2 s per step. The variable temperature patterns were collected with a data collection time of 1 s per step. For variable temperatures, the sample was placed on a zero-background diffraction plate and heated to 50 °C, 100 °C, 150 °C and 200 °C, respectively, for 1 h and PXRD data were collected. The room temperature data were fit to the single crystal data and possible metaschoepite via the Le Bail method.

Fourier transform infrared (FTIR) and Raman spectroscopy. FTIR data were undertaken on a Bruker Vertex 70 with a diamond ATR crystal. The spectrum was recorded over 4000–400 cm^{-1} range. Raman spectrum was collected on a

Renishaw inVia spectrometer equipped with a 785 nm Ar laser in the range of 2000–100 cm^{-1} with a spectral resolution of ~1.7 cm^{-1}.

Diffuse reflectance spectroscopy (DRS). The absorption spectra in the UV-visible region were recorded on an Agilent Cary 5000 spectrophotometer equipped with a Labsphere Biconical Accessory and referenced to a Labsphere certified standard.

Thermogravimetric and differential thermal analysis (TG/DTA). TG/DTA was performed on a Netzsch STA449F3 at a heating rate of 10 °C min^{-1} under air flow at a rate of 50 cm^3 min^{-1}.

3. Results and discussion

3.1. Material synthesis and characterisation

A series of hydrothermal syntheses were performed to address the formation and stabilization of **U-N1** with various solution pHs. Without pH adjustment, the synthesis (starting solution pH 3.32 and final pH 2.84) led to the formation of **U-N1** in low yield (~27 wt%). Gradually adjusting the starting solution pH to 4.0, 4.5 and 5.0 with a diluted NH$_3$ solution increased the yield but with reduced crystal sizes. Further increasing the solution pH to above 5.0 led to the formation of a fine amorphous phase with a cloudy solution. As such, the optimized starting solution pH range for the synthesis of **U-N1** would be between 4.0 and 5.0, with a trade-off between crystal quality and yield as pH increases across this range.

The room temperature PXRD pattern of **U-N1** matched the pattern simulated from the single crystal data, suggesting a pure phase material was obtained (Fig. S1, ESI†). The SEM-EDS examination of **U-N1** confirmed the thin plate crystal morphology and the presence of U, N and O, with a U : N atomic ratio 1 : 1 (Fig. 1 and Table S1, ESI†). Note the quantification of O by EDS can be inaccurate and, as such, the O stoichiometry is likely to be underrepresented.

3.2. Crystal structure and discussion

The single crystal data and structure refinement details for **U-N1** are summarised in Table 1, with selected bond lengths (Å) and angles (°) listed in Table 2. **U-N1** crystallises in the orthorhombic $Pmn2_1$ space group. It has a layered crystal structure (Fig. 2 and Fig. S2, ESI†) based on α-U$_3$O$_8$ type uranium oxide hydroxide layers (Fig. 2b) and interlayer $(NH_4)^+$ cations and $(NO_3)^-$ anions (Fig. 2a). There are two distinct uranyl centres in pentagonal bipyramidal coordination geometry, with U–O bond lengths from 1.802(10) to 1.840(17) Å and normal O–U–O angles from 178.4(7) to 179.0(6)°, and five U–O bonds in the equatorial plane range from 2.255(11) to 2.631(17) Å. The uranium polyhedra share edges to form the α-U$_3$O$_8$ type uranium oxide hydroxide layer (Fig. 2b). Both $(NH_4)^+$ cations and $(NO_3)^-$ anions are located between the uranyl oxide hydroxide layers, with N–O bonds of the $(NO_3)^-$ anion ranging from 1.259(19) to 1.26(4) Å. The distance between

Table 1 Crystal data and structure refinements for **U-N1**

Compound	**U-N1**
CCDC	2353965
Formula	H$_{10}$N$_3$O$_{14}$U$_3$
Formula weight	990.20
Crystal system	Orthorhombic
Space group	$Pmn2_1$
a (Å)	12.387(3)
b (Å)	7.4410(15)
c (Å)	7.0020(14)
α (°)	90
β (°)	90
γ (°)	90
Volume (Å^3)	645.4(2)
Z/μ (mm^{-1})	2/37.627
Min./max. θ [°]	2.738/24.989
d_{calcd} (g cm^{-3})	5.085
GOF	1.006
Final $R_1{}^a$ [$I > 2\sigma(I)$]	0.0346
Final w$R_2{}^b$ [$I > 2\sigma(I)$]	0.0869
Flack parameter	0.006(18)

$^a R_1 = \sum ||F_o| - |F_c|| / |F_o|$. $^b wR_2 = \{\sum[w(F_o{}^2 - F_c{}^2)^2]/\sum[w(F_o{}^2)^2]\}^{1/2}$.
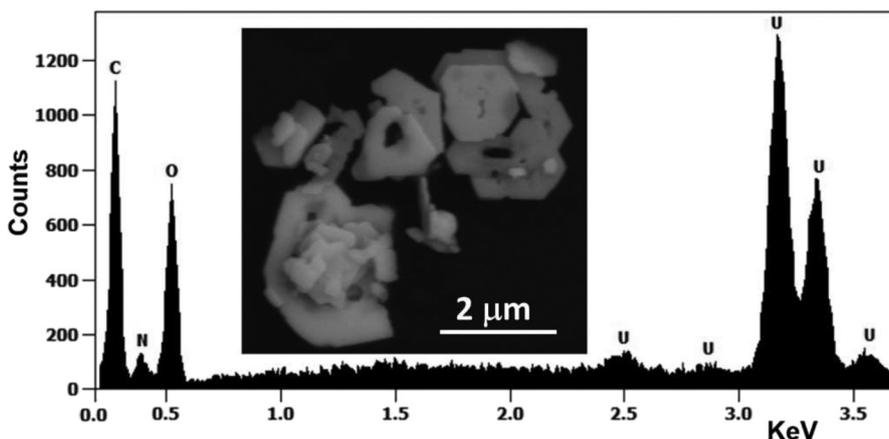

Fig. 1 A backscattered SEM image of **U-N1** inset in the corresponding EDS spectrum.

Table 2 Selected bond lengths and angles for compound **U-N1**

Bond	Length (Å)	Bond	Length (Å)	Bond	Length (Å)
U1–O1	1.802(10)	U1–O4[b]	2.613(12)	U2–O4[d]	2.397(14)
U1–O2	1.814(12)	O1–U1–O2	179.0(6)	U2–O4[e]	2.397(14)
U1–O3	2.268(12)	U2–O6	1.815(17)	U2–O5	2.631(17)
U1–O3[a]	2.270(11)	U2–O7	1.840(17)	O6–U2–O7	178.4(7)
U1–O5	2.462(5)	U2–O3	2.255(11)	O8–N1	1.259(19)
U1–O4	2.465(13)	U2–O3[c]	2.255(11)	O9–N1	1.26(4)

[a] $\frac{1}{2} - X$, $1 - Y$, $-\frac{1}{2} + Z$. [b] $\frac{1}{2} - X$, $1 - Y$, $\frac{1}{2} + Z$. [c] $1 - X$, $+Y$, $+Z$. [d] $1 - X$, $+Y$, $1 + Z$. [e] $+X$, $+Y$, $1 + Z$.

layers is ~4.01 Å. The possible hydrogen bonds calculated using PLATON are listed in Table S2, ESI†. It is apparent that the $(NH_4)^+$ cation is involved in extensive hydrogen bonding with uranyl oxygens, herein called O$_{-yl}$, (O1 and O2) and O (O3) inside the layer (Fig. 2c). In addition, the $(NO_3)^-$ anion also has hydrogen bonding with $(NH_4)^+$ cation and, through this, also a uranyl oxygen (O7) (Fig. 2d). In the interlayer, $(NH_4)^+$ and $(NO_3)^-$ in 2 : 1 ratio are packed into a layer via hydrogen bonding (H⋯O8/O9) (Table S2 and Fig. S2, ESI†).

The bond valence sum (BVS) calculations (Table S3, ESI†), using literature values for U(VI) ($R_{U-O} = 2.051$; $B = 0.519$),[49] indicated that both U centres are present as U(VI) [U1 (5.76 vu) and U2 (5.81 vu)]. The unit cell contains 2N, 6U and 30O (Table 1), with the majority as O and two OH [O4 (1.28) and O5 (0.77)].

As such, the formula for **U-N1** was determined to be $(NH_4)_2(NO_3)[(UO_2)_3O_2(OH)_3]$.

3.3. The role of ammonium ions

Unlike alkali metal ions (e.g., Na$^+$ and K$^+$), which are readily bonded to nearby O$_{-yl}$ and possibly OH and H$_2$O extending into the interlayer, the $(NH_4)^+$ cation is only involved in H-bonding with adjacent O-donors. It is clear from Table S2, ESI† that the $(NH_4)^+$ cation is involved in possible H-bonding with O$_{-yl}$ (O1, O2, O6 and O7), O (O3) and the nitrate anion (O8 and O9). Such interactions between $(NH_4)^+$ cation and the nitrate anion at the interlayer facilitate the inclusion of the nitrate anions.

3.4. Anion inclusion in UOH materials

The anion inclusion in UOH materials is much less studied. A recent work reported the inclusion of $(IO_3)^-$ anions in a synthetic UOH material.[41] In that study, $Rb_2K_2[(UO_2)_6O_4(OH)_6]\cdot(IO_3)_2$ was synthesized hydrothermally at 220 °C using uranyl acetate, KIO$_3$ and RbIO$_3$ as precursors with initial solution pH 5. The compound crystallised in the trigonal space group $P3_1m$ ($a = 7.1406(5)$ Å and $c = 7.4646(7)$ Å), has a layered structure with α-U$_3$O$_8$ layers and interlayer K(I) and Rb(I) ions, as well as $(IO_3)^-$ anions. In this work, compound **U-N1** crystallised in orthorhombic space group $Pmn2_1$ ($a = 12.387(3)$ Å, $b = 7.4410(15)$ Å and $c = 7.0020(14)$ Å) has a
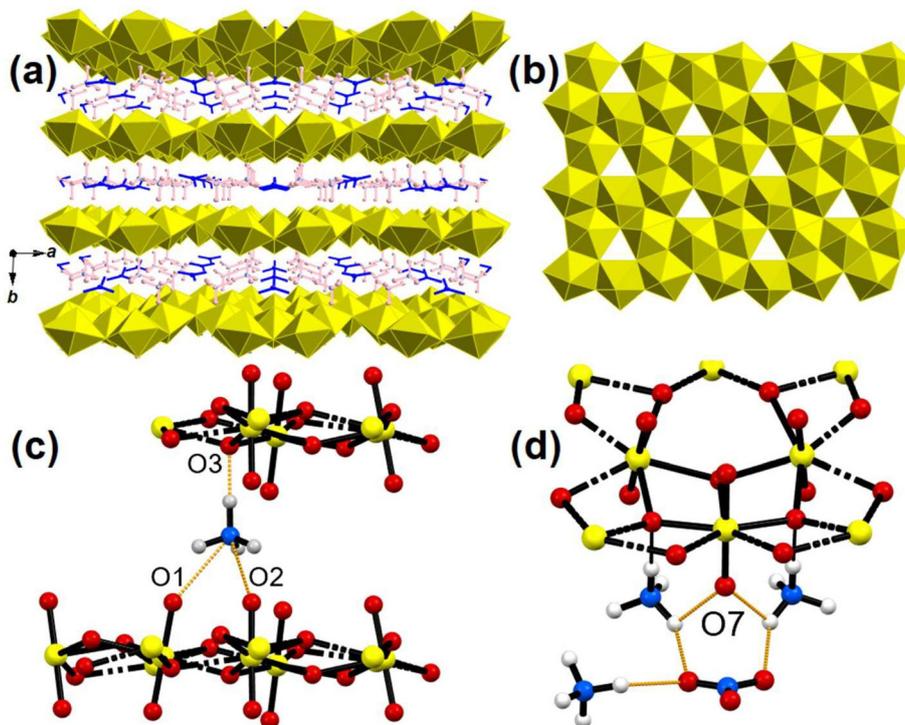

Fig. 2 Crystal structure of **U-N1**: a polyhedral view of the layered structure with interlayer $(NH_4)^+$ cations in pink and $(NO_3)^-$ anions in blue (a), α-U$_3$O$_8$ type uranium oxide hydroxide layer (b), hydrogen bonding of $(NH_4)^+$ with O$_{-yl}$ (O1 and O2) and O (O3) (c), and hydrogen bonding between $(NH_4)^+$ and $(NO_3)^-$ as well as O7 (d), U in yellow, O in red, N in blue and potential hydrogen bonds in orange lines.

similar layered structure with α-U_3O_8 layers but with incorporation of both $(NH_4)^+$ ions and $(NO_3)^-$ anions.

3.5. Electronic structures

The electronic structure of **U-N1** was investigated using DRS. The DRS spectrum (Fig. 3) shows the broad and unresolved absorption bands in the UV region (300 nm–500 nm) with two strong maxima at ~320 and 355 nm, and further two medium maxima at ~425 and 480 nm, corresponding to the typical U–O charge transfer bands for the U(VI) containing materials.[50,51]

3.6. Vibrational modes

The linear $(UO_2)^{2+}$ group has three fundamental vibrational modes, namely the Raman active ν_1 – symmetric stretching vibration, and two infrared active modes: ν_2 – doubly degenerate bending vibration and ν_3 – antisymmetric stretching vibration.[52] The decrease of uranyl group symmetry could result in the splitting of the $\nu_2(UO_2)^{2+}$ and in activation of the $\nu_1(UO_2)^{2+}$ in the infrared spectrum and of $\nu_3(UO_2)^{2+}$ in the Raman spectrum.[52]

The Raman spectrum of compound **U-N1** (Fig. 4a) revealed two strong bands at 841 and 827 cm^{-1} attributed to the $\nu_1(UO_2)^{2+}$ symmetric stretching vibrations.[53,54] These wavenumbers correspond to calculated U–O bond lengths of 1.770 Å to 1.784 Å for the uranyl centres,[55] slightly shorter than the observed U–O bond lengths [1.802(10) Å–1.840(17) Å] determined from the crystal structure. Two medium-intensity Raman bands at 555 and 453 cm^{-1} are predominantly due to (U_3O) bridge and $(U-O_{ligand})$ stretching vibrations.[52] Weak bands below 350 cm^{-1} could be due to various bending vibration modes, molecular deformation, and lattice modes.[52] The presence of nitrate anions was confirmed with the characteristic Raman peak located at 1046 cm^{-1} assigned to the ν_1 (NO_3) symmetric stretching vibration (Fig. 4a).[56] Furthermore, two shoulders located on the lower frequency side of the
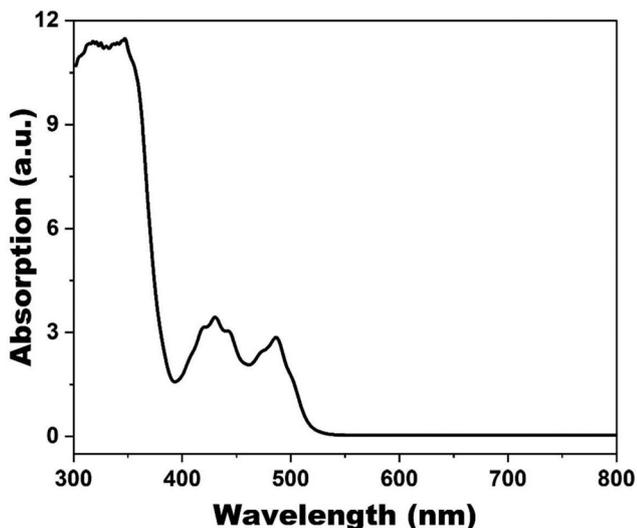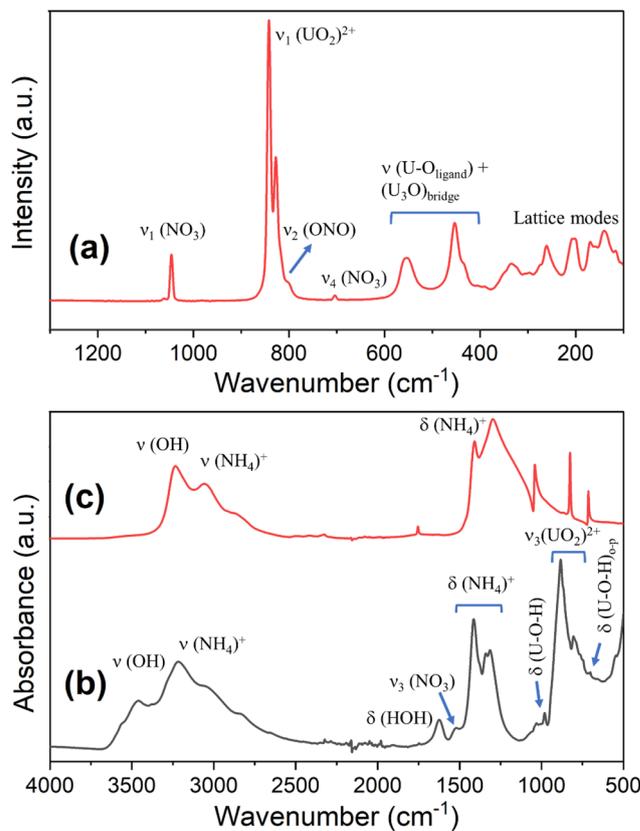

Fig. 4 Vibrational spectra of compound **U-N1**: Raman (a), FTIR (b) together with FTIR of $(NH_4)NO_3$ (c) as a reference.

uranyl peak (~817 and 804 cm^{-1}) and a weak Raman peak at 704 cm^{-1} may be assigned to the ν_2 ONO and ν_4 (NO_3) bending modes, respectively.

The FTIR spectrum of compound **U-N1** (Fig. 4b), in comparison with that of $(NH_4)NO_3$ (Fig. 4c), showed characteristic bands for both the expected UOH phase and $(NH_4)NO_3$, confirming that the assignment of $(NH_4)NO_3$ as the interlayer species is correct. The characteristic infrared bands for a typical UOH phase are: $\nu(OH)$ – stretching vibrations of hydroxyl ions (including water molecules) in the region 3600–3460 cm^{-1}; the corresponding bending vibrations of $\delta(U–O–H)$ around 1030–980 cm^{-1}, and bands in the range 760–700 cm^{-1}, presumed to mostly be due to out-of-plane bending vibrations of U–O–H. Two strong infrared peaks at 883 and 805 cm^{-1} were attributed to the $\nu_3(UO_2)^{2+}$ antisymmetric stretching vibrations. There are several characteristic infrared bands for $(NH_4)NO_3$: the strong, broad bands at ~3200 cm^{-1} are typical of the absorption of the $(NH_4)^+$ ions, with the corresponding bending modes evident in the region 1415–1315 cm^{-1}. Additionally, the bending vibration mode of HOH is centred around 1624 cm^{-1} and a weak IR peak at 1524 cm^{-1} is due to $\nu_3(NO_3)$ antisymmetric stretching vibrations.

The combination of micro-Raman and FTIR makes it evident that present in the compound **U-N1** are the expected

Fig. 3 A DRS spectrum of **U-N1** in the UV-vis region.

uranyl and hydroxyl vibrations typical for a UOH phase, but also containing additional spectral features that can be assigned to the presence of both $(NH_4)^+$ and $(NO_3)^-$ consistent with the structure assigned using SC-XRD.

3.7. Thermal stability

The thermal stability of compound **U-N1** was also investigated. From the thermogravimetric (TG) and 1st derivatives curves (Fig. S3, ESI†), **U-N1** lost about 9.4 wt% absorbed H_2O (equivalent to 5–6 lattice H_2O molecules per formula) up to 200 °C, followed by the gradual decomposition of $(NH_4)^+$ and $(NH_4)NO_3$ from 200 °C to 450 °C, then losing NO_2 and $(OH)^-$ from 500 °C to 700 °C, losing O to form UO_2 as the final residue at ~800 °C (calc. 75.0%; obs. 74.7%).

The higher temperature at which much of the water was lost is strongly indicative of their inclusion in the crystal lattice of **U-N1**. Due to their disorder, such waters would not be visible in SC-XRD and, as such, variable temperature PXRD experiment was performed in order to elucidate the impact of these water molecules on stabilising the structure. PXRD data were collected after successively heating **U-N1** to 50 °C, 100 °C, 150 °C and 200 °C. The patterns (Fig. S4, ESI†) reveal that the structure remains unchanged at 100 °C, after which a complete decomposition occurs, as evidenced by only broad undefined peaks remaining visible in the PXRD patterns at 150 °C and 200 °C. This strongly suggests that the lattice water plays a crucial role in stabilising the structure, likely involving H-bonding interactions in addition to those proposed (Table S2, ESI†) between the U_3O_8-type layers involving NH_4^+ and NO_3^- species in the interlayer.

3.8. Implications and perspectives

U geochemistry/UOH minerals. Understanding the alteration chemistry of uranium oxides in the presence of ammonium ions is vital, given their abundance in the environment. With only a couple of synthetic UOH materials containing ammonium ions being structurally characterised, there exists an obvious need for further work to better understand the effect of ammonium on the formation and stabilization of various UOH structure types across a wide range of synthesis parameters such as solution pH, ammonium concentration, temperature *etc.* We can speculate that NH_4^+ is commonly present in the natural uranyl-oxide hydroxy-hydrate minerals and has been overlooked so far due to the fact that (1) nobody considered that NH_4^+ could be present in these minerals and, as such, their presence was overlooked, or (2) experimental difficulties in the determination of its content (namely because the older generations of the solid-state detectors used for EDS were not-good-enough to detect credibly emission lines in the low-energy part of the spectrum). UOH minerals are abundant products of the oxidation-hydration weathering of uraninite and they commonly occur in the mineral associations involving sulfate minerals formed under acidic conditions. These mineral associations are related to the acid-mine-drainage (AMD) environments,[57] where microbial activity often occurs and thus, we can expect nitrogen to be present in

the alteration system. Furthermore, several minerals and unnamed phases have been reported,[57] with particularly suspicious low-cation populations (cation-deficiencies). Such observations most commonly concern minerals containing K^+ as a dominant cation, and thus, it is highly probable that NH_4^+ might be present to compensate for the cation deficiency.

Possible SNF alteration pathway. Under geological disposal, SNF might be exposed to fluids rich in ammonium. As such, the effect of ammonium on the alteration pathway of SNF is important and should be comprehensively investigated. In addition to the sole effect of ammonium ions, dual-cation UOH systems with alkali and alkaline earth metal ions, and ammonium ions are also important due to their relative abundances in the geological environment. Given that no synthetic UOH material with dual cations involving ammonium ions has been reported, it clearly emphasises the need to explore such UOH systems further.

Apart from SNF, other uranium-rich radioactive wastes are also generated from the nuclear fuel cycle such as depleted uranium from the U-235 enrichment for fuel fabrication, and nuclear medicine sector such as the production of Mo-99 *via* nuclear fission of U-235 targets in reactors.[58] They require proper treatment and conditioning to form solid waste forms for geological disposal.[58] Like the circumstance for SNF under geological disposal, all other uranium-rich waste forms might also be exposed to fluids rich in ammonium. As such, further research is necessary to understand better the effect of ammonium ions on the alteration of various uranium-rich waste forms.

4. Conclusions

Although ammonium exists in high concentrations in nature, its role on the formation and stabilization of UOH minerals and synthetic phases is not well defined. This work accounts for the first in the limited synthetic studies trying to reveal the role of ammonium ions in UOH systems.[29] Consequently, a UOH phase containing α-U_3O_8 layers and interlayer $(NH_4)^+$ ions, introduced *via* the inclusion of $(NH_4)NO_3$, was successfully synthesized under mild hydrothermal conditions and characterised using both structural and spectroscopic techniques. While a combination of micro-Raman and FTIR provided evidence for the presence of uranyl and $(NH_4)^+$ cations along with OH^- and $(NO_3)^-$ anions, synchrotron single crystal XRD revealed the role of $(NH_4)^+$ ions as a single charge cation involved in extensive hydrogen bonding with both the α-U_3O_8 type layer and also neighbouring nitrate anions, facilitating their inclusion into the interlayer.

The findings have implications for uranium geochemistry, possible SNF alteration pathway under geological disposal, and the treatment of wastes arising from nuclear fuel fabrications. Further work is necessary to establish the role of $(NH_4)^+$ ions in the stabilisation of UOH materials at lower temperatures and their utilisation as a means of possible inclusion for

anions of interest across a wide range of experimental parameters.

Author contributions

YZ: concept, resource, project management, supervision, data curation, data analysis, paper drafting; TAA/MKN/IK: data curation, data analysis, paper drafting; JP: concept, data analysis, paper drafting.

Data availability

Data can be made available through a request to the corresponding author.

Conflicts of interest

The authors are not aware of any conflict of interest.

Acknowledgements

References

1 P. C. Burns, Hydrated uranium oxides, in *Comprehensive Nuclear Materials*, ed. R. Konings and R. Stoller, Elsevier, 2nd edn, 2020.
2 Y. Zhang, K. T. Lu and R. Zheng, *Dalton Trans.*, 2022, **51**, 2158–2169.
3 (*a*) R. J. Baker, *Coord. Chem. Rev.*, 2014, **266**, 123–136; (*b*) J. Plášil, *J. Geosci.*, 2014, **59**, 99–114.
4 J. Plášil, *Eur. J. Mineral.*, 2017, **29**, 1–15.
5 R. J. Finch and R. C. Ewing, *J. Nucl. Mater.*, 1992, **190**, 133–156.
6 J. Janeczek and R. Ewing, *J. Nucl. Mater.*, 1992, **190**, 157–173.
7 T. A. Olds, J. Plášil, A. R. Kampf, T. Spano, P. Haynes, S. M. Carlson, P. C. Burns, A. Simonetti and O. P. Mills, *Am. Mineral.*, 2018, **103**, 143–150.
8 K.-A. Hughes, P. C. Burns and U. Kolitsch, *Can. Mineral.*, 2003, **41**, 677–685.
9 K. T. Lu, Y. Zhang, T. Wei, J. Čejka and R. Zheng, *Dalton Trans.*, 2020, **49**, 5832–5841.
10 P. C. Burns and J. Hanchar, *Can. Mineral.*, 1999, **37**, 1483–1491.
11 (*a*) M. L. Miller, R. J. Finch, P. C. Burns and R. C. Ewing, *J. Mater. Res.*, 1996, **11**(12), 3048–5056; (*b*) S. V. Krivovichev and J. Plášil, *CHAPTER 3: Mineralogy and crystallography of uranium*, Mineralogical Association of Canada Short Course 43, Winnipeg MB, 2013, 15–119.
12 P. C. Burns and F. C. Hill, *Can. Mineral.*, 2000, **38**, 163–173.
13 F. C. Hill and P. C. Burns, *Can. Mineral.*, 1999, **37**, 1283–1288.
14 R. E. Glatz, Y. Li, K.-A. Hughes, C. L. Cahill and P. C. Burns, *Can. Mineral.*, 2002, **40**, 217–224.
15 P. C. Burns and F. C. Hill, *Can. Mineral.*, 2000, **38**, 175–181.
16 K. T. Lu, Y. Zhang, T. Wei, T. A. Ablott, T. H. Nguyen and R. Zheng, *New J. Chem.*, 2022, **46**, 1371–1380.
17 K. T. Lu, Y. Zhang, T. Wei, T. A. Ablott, J. Plasil, I. Karatchevtseva and R. Zheng, *New J. Chem.*, 2023, **47**, 13286–13296.
18 Y. Zhang, K. T. Lu, T. Wei, I. Karatchevtseva and R. Zheng, *Dalton Trans.*, 2023, **52**, 17942–17953.
19 M. Rivenet, N. Vigier, P. Roussel and F. Abraham, *J. Solid State Chem.*, 2009, **182**, 905–912.
20 N. G. Chernorukov, O. V. Nipruk, K. A. Klinshova, O. N. Tumaeva and D. V. Sokolov, *New J. Chem.*, 2021, **45**, 9922–9935.
21 T. A. Ablott, K. T. Lu, T. Wei and Y. Zhang, *Dalton Trans.*, 2023, **52**, 6629–6640.
22 Y. Zhang, J. Čejka, G. R. Lumpkin, T. T. Tran, I. Aharonovich, I. Karatchevtseva, J. R. Price, N. Scales and K. Lu, *New J. Chem.*, 2016, **40**, 5357–5357.
23 Y. Li and P. C. Burns, *Can. Mineral.*, 2000, **38**, 1433–1441.
24 Y. Zhang, R. Aughterson, I. Karatchevtseva, L. Kong, T. T. Tran, J. Čejka, I. Aharonovich and G. R. Lumpkin, *New J. Chem.*, 2018, **42**, 12386–12393.
25 Y. Zhang, R. D. Aughterson, Z. Zhang, T. Wei, K. Lu, J. Čejka and I. Karatchevtseva, *Inorg. Chem.*, 2019, **58**, 10812–10821.
26 Y. Zhang, K. T. Lu, T. A. Ablott, T. Wei and R. Zheng, *Chem. – Asian J.*, 2024, **19**, e202400101.
27 K.-A. Kubatko and P. C. Burns, *Inorg. Chem.*, 2006, **45**, 10277–10281.
28 Y. Zhang, T. Wei, T. T. Tran, K. T. Lu, Z. Zhang, J. R. Price, I. Aharonovich and R. Zheng, *Inorg. Chem.*, 2020, **59**, 12166–12175.
29 Y. Li, C. L. Cahill and P. C. Burns, *Chem. Mater.*, 2001, **13**, 4026–4031.
30 T. A. Ablott, K. T. Lu, R. D. Aughterson and Y. Zhang, *Dalton Trans.*, 2022, **51**, 15965–15973.
31 K. T. Lu, Y. Zhang, T. Wei, Z. Wang, D. T. Oldfield and R. Zheng, *Inorg. Chem.*, 2021, **60**, 13233–13241.
32 K. T. Lu, Y. Zhang, R. D. Aughterson and R. Zheng, *Dalton Trans.*, 2020, **49**, 15854–15863.

33 S. Paik, S. Biswas, S. Bhattacharya and S. B. Roy, *J. Radioanal. Nucl. Chem.*, 2013, **295**, 2141–2146.

34 (*a*) B. Tomazic and M. Branica, *J. Inorg. Nucl. Chem.*, 1972, **34**, 1319–1332; (*b*) J. Sutton, *J. Inorg. Nucl. Chem.*, 1955, **1**, 68–74; (*c*) J. Maly and V. Vesely, *J. Inorg. Nucl. Chem.*, 1958, **7**, 119–128.

35 J. B. Ainscough and B. W. Oldfield, *J. Appl. Chem.*, 2007, **12**(9), 418–424.

36 S. Manna, S. B. Roy and J. B. Joshi, *J. Nucl. Mater.*, 2012, **424**, 94–100.

37 S. Paik, S. Biswas, S. Bhattacharya and S. B. Roy, *J. Nucl. Mater.*, 2013, **440**, 34–38.

38 J. Jo, T. Yamanaka, T. Kashimura, Y. Okunishi, Y. Kuwahara, I. Kadota, Y. Miyoshi, J.-I. Ishibashi and H. Chiba, *Geochem. J.*, 2018, **52**, 317–333.

39 J. Friedl, D. De Rosa, D. W. Rowlings, P. R. Grace, Ch. Müller and C. Scheer, *Soil Biol. Biochem.*, 2018, **125**, 340–349.

40 Mineral data: **https://www.mindat.org/chemsearch.php?inc=N%2CU%2C&exc=&ima=0&sub=Search±for±Minerals** (accessed on the 8th of May 2024).

41 G. L. Murphy, P. Kegler, M. Klinkenberg, A. Wilden, M. Henkes, D. Schneider and E. V. Alekseev, *Dalton Trans.*, 2021, **50**, 17257–17264.

42 D. Aragão, J. Aishima, H. Cherukuvada, R. Clarken, M. Clift, N. P. Cowieson, D. J. Ericsson, C. L. Gee, S. Macedo, N. Mudie, S. Panjikar, J. R. Price, A. Riboldi-Tunnicliffe, R. Rostan, R. Williamson and T. T. Caradoc-Davies, *J. Synchrotron Radiat.*, 2018, **25**, 885–891.

43 W. Kabsch, *Acta Crystallogr., Sect. D: Biol. Crystallogr.*, 2010, **66**, 133–144.

44 G. M. Sheldrick, *SADABS, Empirical Absorption and Correction Software*, Göttingen, University of Göttingen, 1996.

45 G. M. Sheldrick, *Acta Crystallogr., Sect. A: Found. Adv.*, 2015, **71**, 3–8.

46 G. M. Sheldrick, *Acta Crystallogr., Sect. C: Struct. Chem.*, 2015, **71**, 3–8.

47 O. V. Dolomanov, L. J. Bourhis, R. J. Gildea, J. A. K. Howard and H. Puschmann, *J. Appl. Crystallogr.*, 2009, **42**, 339–341.

48 A. L. Spek, *Acta Crystallogr., Sect. D: Biol. Crystallogr.*, 2009, **D65**, 148–155.

49 (*a*) I. D. Brown, *Chem. Rev.*, 2009, **109**(12), 6858–6919; (*b*) P. C. Burns, P. C. Burns, R. C. Ewing and F. C. Hawthorne, *Can. Mineral.*, 1997, **35**, 1551–1570.

50 (*a*) N. D. Shepherd, Y. Zhang, I. Karatchevtseva, J. R. Price, L. Kong, N. Scales and G. R. Lumpkin, *Polyhedron*, 2016, **113**, 88–95; (*b*) Y. Zhang, D. J. Fanna, N. D. Shepherd, I. Karatchevtseva, K. Lu, L. Kong and J. R. Price, *RSC Adv.*, 2016, **6**, 75045–75053.

51 (*a*) E. R. Vance, Y. Zhang and Z. Zhang, *J. Nucl. Mater.*, 2010, **400**(1), 8–14; (*b*) Y. Zhang, T. Wei, Z. Zhang, L. Kong, P. Dayal and D. J. Gregg, *J. Am. Ceram. Soc.*, 2019, **102**(12), 7699–7709.

52 R. L. Frost, J. Čejka and M. L. Weier, *J. Raman Spectrosc.*, 2007, **38**(4), 460–466.

53 (*a*) Y. Zhang, L. Kong, I. Karatchevtseva, R. D. Aughterson, D. J. Gregg and G. Triani, *J. Am. Ceram. Soc.*, 2017, **100**(9), 4341–4351; (*b*) Y. Zhang, L. Kong, R. D. Aughterson, I. Karatchevtseva and R. Zheng, *J. Am. Ceram. Soc.*, 2017, **100**(11), 5335–5346.

54 (*a*) Y. Zhang, J. Čejka, I. Karatchevseva, M. Qin, L. Kong, K. Short, S. C. Middleburg and G. R. Lumpkin, *J. Nucl. Mater.*, 2014, **446**, 68–72; (*b*) Y. Zhang, I. Karatchevtseva, M. Qin, S. C. Middleburgh and G. R. Lumpkin, *J. Nucl. Mater.*, 2013, **437**, 149–153.

55 J. R. Bartlett and R. P. Cooney, *J. Mol. Struct.*, 1989, **193**, 295–300.

56 G. Socrates, *Infrared and Raman Characteristic Group Frequencies: Tables and Charts*, John Wiley & Sons Hoboken, NY, 3rd edn, 2001.

57 (*a*) J. Brugger, N. Meisser and P. C. Burns, *Am. Mineral.*, 2003, **88**, 676–685; (*b*) J. Plášil, J. Sejkora, R. Škoda and P. Škácha, *J. Geosci.*, 2014, **59**, 223–253; (*c*) J. Plášil, G. Steciuk, J. Majzlan, R. Škoda, J. Filip, M. Petr, J. Kolařík, M. Klementová, O. Bähre, G. Klöß and L. Lapčák, *ACS Earth Space Chem.*, 2022, **6**(5), 1250–1258.

58 (*a*) Y. Zhang, L. Kong, M. Ionescu and D. J. Gregg, *J. Eur. Ceram. Soc.*, 2022, **42**(5), 1852–1876; (*b*) Y. Zhang and A. H. Mir, *J. Nucl. Mater.*, 2023, **583**, 154512.